Theory of ballistic electron emission microscopy

D. A. Pearson and L. J. Sham
Department of Physics 0350, University of California, San Diego, La Jolla, California 92093-0350
(Received 20 November 2000; revised manuscript received 27 March 2001; published 10 September 2001)

A theory of ballistic electron emission microscopy is presented that incorporates constant-tunnel-current feedback and models the band-structure and space-charge effects on the electron transmission. The computation is beyond the effective-mass approximation but short of being from first principles. The transmission coefficient includes detailed symmetry treatments of the Γ-, L-, and X-point semiconductor conduction channels and the three-dimensional k-space current injection dependency. This approach naturally leads to the inclusion of multiple current channels, i.e., simultaneous inclusion of several propagating and evanescent bands of various symmetry types. We investigate the effects of the model parameters on the I-V spectra and compare our predictions to experiment, yielding fairly good agreement. We also compare theoretical and experimental Au/GaAs(001) dI/dV data and find that the L point does not contribute to an observable threshold and that the corresponding experimental feature is due instead to band-structure effects.

DOI: 10.1103/PhysRevB.64.125408 PACS number(s): 73.23.Ad, 73.40.Ns

I. INTRODUCTION

Since its initial development ballistic electron emission microscopy[1,2] (BEEM) has been the subject of a considerable amount of research.[3–19] However, the bulk of the published work to date has been focused on the experimental aspects of BEEM. Only a limited number of theoretical treatments[20] have been put forth, in terms of which nearly all of the experimental data have been interpreted; in particular, Ref. 2 or modifications thereof.[8,9,14,16,17,21,22] These models have gained favor within the experimental community due in part to their successes in describing BEEM-related phenomena, and to the relative ease with which they can be employed in the interpretation of the data. There are, however, a number of key physical effects that were not addressed in these earlier models. These we will examine in this paper. Our goal is to develop a comprehensive BEEM theory that includes all important physical effects.

The first physical effect that we included in our model is constant-tunnel-current feedback. This necessitates that we accurately calculate any two of the three BEEM currents, i.e., the base, collector, and tunnel currents. Current conservation determines the third. The I-V spectra for the models cited are obtained in the constant-height mode, i.e., for fixed tip/metal-overlayer separation. Experiments, on the other hand, are commonly carried out in constant-tunnel-current mode, i.e., for fixed tunnel current and *variable* tip/metal-overlayer separation as a function of voltage. (Calculation of absolute magnitudes of the currents is nonexistent in the earlier models, as is modeling of the constant-tunnel-current feedback.)

In addition, we incorporated a number of other physical effects that have either been included separately in a limited fashion or not at all. The effects we included are as follows. (1) Detailed tip-shape effects on the vacuum potential—in the earlier models tip-shape effects are accounted for only in a very rough manner, by uniformly reducing the height of the vacuum potential by the average of the bias over the vacuum. (2) A metal-overlayer thickness dependence. (3) Semiconductor dielectric and doping dependencies as well as the effect of temperature on the Schottky-barrier-potential shape. (4) Tunneling through the Schottky barrier and the space-charge layer—a flat, very wide barrier is used in most of the previous models which effectively precludes tunneling. (In very lightly doped semiconductors this is a reasonable approximation but very lightly doped semiconductors are rarely used.) (5) A detailed transmission coefficient calculation that couples via boundary conditions the scanning tunneling microscope (STM) tip, vacuum, metal overlayer, semiconductor, and the metal-collector electrode—in the earlier models usually only the vacuum[23] and the metal-overlayer/semiconductor[2,8,24] interface were analyzed in any detail. (6) Inclusion of three-dimensional k-space effects, especially as regards the semiconductor bands. (7) Inclusion of the wave-function symmetries and parallel-momentum requirements of the Γ, L, and X conduction channels. (8) Incorporation of the corresponding evanescent wave functions—which are typically present when more than one nondegenerate band is considered—to the boundary condition matching at the various material interfaces. And (9) inclusion of phenomenological damping in the metal overlayer, semiconductor, and the oxide layer between these two materials, if present. All of the above features are incorporated into the transmission coefficient by way of the transfer-matrix method.[25–27]

A brief summary of the key results was presented in Ref. 28.

In Sec. II the salient features of our BEEM theory are presented. The theory is then used in Sec. III to make various I-V spectral predictions regarding experimentally controllable quantities, e.g., the effects of doping, temperature, metal-overlayer thickness, tip size, tunnel-current bias dependencies, etc., on the corresponding I-V data. Thereafter, a comparison is made between the model results and the available experimental data. Finally, a summary of the work and the corresponding conclusions that were drawn are presented in Sec. IV.

II. BEEM THEORY

The main features and computational results of our model are presented here (for more details see Ref. 29). Specifi-

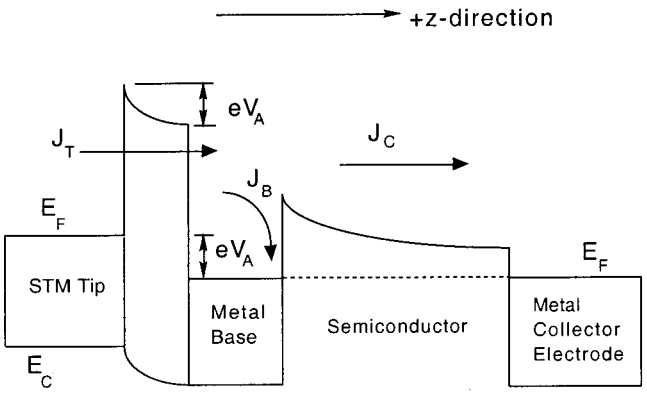

FIG. 1. Energy band diagram used in our BEEM model. J_t, J_b, and J_c are the tunnel-, base-, and collector-current densities, respectively. The nonlinear potential drop across the STM vacuum gap is due to the tip shape. The potential along the symmetry axis is used. The parabolic potential in the semiconductor is due to a uniform space-charge layer, which takes into account the effects of the semiconductor doping and dielectric constant, as well as the temperature, on the barrier size. The tip/base separation is determined by constant-tunnel-current feedback control. The zero of energy is the tip conduction band edge. Current flows along the (001) growth axis. With the exception of the tip, all material interfaces lie parallel to the xy plane.

cally, we discuss how the BEEM current densities are calculated and how they are employed to obtain constant-tunnel-current feedback. We then discuss the process for calculating the Schottky-barrier potential. Next the method used to tackle the issue of symmetry effects at the Γ, L, and X points on the BEEM threshold voltages is outlined. And, finally, we discuss the determination of an effective STM tip area for conversion of the current density into current for comparison with experiment.

A. Current densities and constant-tunnel-current feedback

The injected tunnel current I_t from the STM tip splits into a base current I_b, which returns through the metal overlayer, and a collector current I_c, which traverses the Schottky barrier and returns via the collector electrode (see Fig. 1). Constant-tunnel-current feedback is typically present in a BEEM experiment. To incorporate this feedback we need to calculate any two of the three currents. We calculate the collector and base currents. With the forward propagation direction along the $+z$ axis the net collector-current density J_c is given by

$$J_c = 2\frac{e}{(2\pi)^3}\int T(E_{\vec{k}};V_a)[f(E_{\vec{k}})-f(E_{\vec{k}}+eV_a)]\frac{\hbar k_z}{m_0}d^3\vec{k}, \tag{1}$$

where $\vec{k}$ and $E_{\vec{k}}$ are the allowed electron wave vectors for the system and their corresponding energies, respectively, V_a is the bias voltage, m_0 is the free-electron mass, e is the magnitude of the electron charge, $f(E_{\vec{k}})$ is the probability in the negative electrode that the state $\vec{k}$ is initially occupied, and $T(E_{\vec{k}};V_a)$ is the BEEM transmission coefficient. The factor of 2 is the electron spin degeneracy. We assume that a quasithermal equilibrium exists in both the emitter and collector so that $f(E_{\vec{k}})$ can be replaced by the Fermi distribution function.

Three-dimensional (k_x, k_y, and E) Monte Carlo techniques[30] are used to integrate the collector-current density J_c, Eq. (1) and the base-current density J_b (see Sec. II C 1). Specifically, we integrate over the wave vectors/energies of the electrons in the STM tip, and assume that energy and parallel-momentum conservation hold at all interfaces—except where noted otherwise—to relate all the other wave vectors and energies in the other BEEM components back to the STM tip. The corresponding statistical error, given in the form of a standard deviation, is estimated in the MISER Monte Carlo routine[30] and is presented in each I-V plot. Typically 1000 and 250 sample points were employed in the collector- and base-current density integrations, respectively.

Phenomenological scattering, which reproduces bulk mobilities, is included in $T(E_{\vec{k}};V_a)$ as complex wave vectors in the metal overlayer, oxide layer, and semiconductor. We assume that all the scattered electrons go into the base-current density J_b. Hence, J_b is given by replacing $T(E_{\vec{k}};V_a)$ in Eq. (1) with the corresponding absorption coefficient $A(E_{\vec{k}};V_a)$,

$$A(E_{\vec{k}};V_a)=1-R(E_{\vec{k}};V_a)-T(E_{\vec{k}};V_a), \tag{2}$$

where $R(E_{\vec{k}};V_a)$ is the BEEM reflection coefficient. Similarly, the tunnel-current density J_t, is obtained from J_c by replacing $T(E_{\vec{k}};V_a)$ with $1-R(E_{\vec{k}};V_a)$ (Fig. 1), obeying current conservation.

Given an effective tip area (Sec. II F), the current densities are converted to currents for direct comparison to the experimental BEEM spectra. The tip separation at a given bias is iteratively[31] adjusted such that the calculated tunnel current equals the specified, fixed tunnel current within a predetermined tolerance range. The iteration process is repeated for each increment of voltage, yielding the BEEM spectra in constant-tunnel-current mode.

B. The Schottky-barrier potential

Solving Poisson's equation[32] with the appropriate boundary conditions, assuming uniform doping N_D, and shifting the Schottky barrier from the origin to $z=b$ yields the following expression for the Schottky-barrier-energy profile:

$$\mathcal{E}(z)=\frac{e^2N_D}{2\epsilon}(z-b-z_b)^2+E_F-eV_a+\Delta_{ec}, \tag{3}$$

where the barrier width $z_b=\sqrt{(2\epsilon/e^2N_D)(eV_b-\Delta_{ec})}$ is defined as the value of z where the Schottky electric field is zero. V_b is the Schottky-barrier height relative to the tip Fermi energy E_F. V_a is the applied voltage between the STM tip and the metal overlayer. ϵ is the dielectric constant of the semiconductor. Δ_{ec} is the energy difference between the semiconductor conduction band edge and the Fermi energy. Its value is determined from the difference between the energy gap and the Fermi energy of the semiconductor. The

Fermi energy is determined from the requirement of charge neutrality,[33] i.e., requiring that the sum of the electron and the ionized acceptor concentrations minus the sum of the hole and the ionized donor concentrations be equal to zero. The energy gap is determined using Thurmond's[34] empirically derived temperature dependent equation for GaAs (the semiconductor we will be using in the calculations). Δ_{ec} is a function of temperature and the semiconductor doping level. The shift to $z=b$ is needed to make the position of the Schottky barrier consistent with the rest of the BEEM problem geometry. This potential is incorporated into the model by using the effective-mass approximation (EMA) inside the semiconductor. As a result, Schottky-barrier tunneling is automatically built into the model.

To account for a metal-electrode contact (collector) on the right-hand side of the Schottky barrier, the barrier potential is cut off on this side at a value less than $z=z_b+b$ as specified by the user, and a flat energy profile is employed (Fig. 1). The cutoff length chosen was 100 Å. This is sufficiently thick so that any additional Schottky potential neglected beyond this value is expected to have a negligible tunneling contribution to the collector current. Only those electrons with energy near the top of the Schottky barrier—typically within 0.25 eV—have any appreciable chance of tunneling through it, even if the barrier is heavily doped. The same boundary conditions (see Sec. II A) are employed at both ends of the barrier. (Note that the cutoff length was varied to check that no unwanted artificial reflections resulted from the semiconductor/collector interface. The corresponding collector current decreased when the cutoff was increased and increased when the cutoff was decreased as expected. The attenuation in the semiconductor was sufficient to prevent unwanted artificial reflections from this interface.)

Scattering in the semiconductor is accounted for phenomenologically via the addition of a constant, imaginary wave vector equal to the inverse of the inelastic mean free path length in the semiconductor. However, since the nominal inelastic mean free paths for bulk III-V materials were found to be in the range of 500–1000 Å,[35] which is greater than the semiconductor cutoff length of 100 Å used in the model, we instead use mean free paths in the range of 100–200 Å.

We also include the effects of temperature and doping on the semiconductor scattering via the mobility μ. GaAs mobility data have been obtained by Rode and Knight.[36] They were fitted to a product of power laws,

$$\mu(T,N_D)=\mu_0 T^{\alpha} N_D^{\beta}, \tag{4}$$

where α, β, and μ_0 are fitted to the available data, and N_D and T are given in cm^{-3} and K, respectively. The resultant fits [in $\mathrm{cm}^2/(\mathrm{s\,V})$] are

$$\mu(T,N_D)=5.308\times 10^{11}\ T^{-2.3}\ N_D^{-0.145}\ \text{ for } T\geqslant 58\,^{\circ}\mathrm{K} \tag{5}$$

and

$$\mu(T,N_D)=7.955\times 10^{5}\ TN_D^{-0.145}\ \text{ for }\ T<58\,^{\circ}\mathrm{K}. \tag{6}$$

These fits reasonably reproduce the mobility data over a temperature range from 4 to 1000 K, and doping from near intrinsic, $N_D=10^{14}\ \mathrm{cm}^{-3}$, to near degenerate, $N_D=10^{19}\ \mathrm{cm}^{-3}$.

To relate the mobility to the mean free path l (scattering length as used here), we employ the results of Petritz and Scanlon,[37] i.e.,

$$l\propto \mu T^{1/2}. \tag{7}$$

Using Eq. (7) we obtain an expression relating the initial base-line (see Sec. III A) mean free path l_i at temperature T_i and doping N_{D_i}, to the final mean free path l_f at temperature T_f and doping N_{D_f}, namely,

$$l_f=\frac{\mu_f(T_f,N_{D_f})}{\mu_i(T_i,N_{D_i})}\frac{T_f^{1/2}}{T_i^{1/2}}l_i. \tag{8}$$

C. Γ- and longitudinal *X*-point transmission coefficient analysis

The three lowest conduction band edges (BEEM thresholds) of GaAs in terms of increasing energy occur at the Γ, *L*, and *X* points.[35] For the (001) growth axis, all four *L* valleys are equivalent. The *X* valleys are divided into two transverse ones in the interface plane and one longitudinal one parallel to the growth axis. We calculate the Γ- and longitudinal *X*-point transmission and reflection coefficients via the corresponding wave functions in the various BEEM materials using the transfer-matrix method.[25–27]

1. Γ- and longitudinal X-point wave functions

In the electron propagation through the semiconductor interfaces we require the propagating and evanescent waves. For the contributions from the Γ and *X* valleys we need the energy and the wave functions throughout the zone. We construct a phenomenological model by using 15 plane waves. The Γ-point energies from first-principles band structure calculations are fitted by a phenomenological pseudopotential with symmetrized plane waves.

We use a two-step approach[29] to calculating the wave functions. First, starting from a simple plane-wave basis set about the conventional origin, we begin construction of the symmetrized basis set[38] with the Hamiltonian matrix—in the momentum representation—at the zone center, taking into account the symmetry properties of the crystal lattice; here the GaAs zinc-blende lattice. The plane-wave basis is restricted to the lowest 15 energy waves[39] at the reciprocal lattice vectors $\vec{G}$.[40] The potential terms in the Hamiltonian are evaluated using pseudopotential theory.[41–43] With the Hamiltonian matrix evaluated, we next calculate the corresponding eigenenergies and eigenvectors, thereby completing the determination of the symmetrized wave-function basis at the zone center.

The second part of the approach consists of constructing a full-zone $\vec{k}\cdot\vec{p}$ Hamiltonian matrix,[44] using as a basis the previously determined 15 symmetrized wave functions at the zone center. The $\vec{k}\cdot\vec{p}$ matrix elements are adjusted to pro-

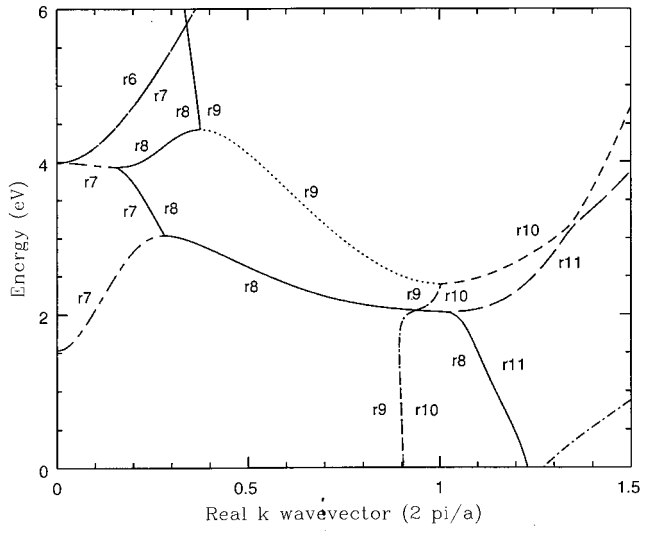

FIG. 2. Energy vs the real part of k_z at $k_x=k_y=0$ for GaAs. The zone edge lies at $k_z=G$. The top of the valence band is at $E=k_z=0$. Here the "real lines," (Ref. 45) those bands with a nonzero imaginary part, are the four *pairs* of vertical or near vertical lines labeled $r7$ through $r11$. (Bands $r6$ and $r7$ for $E>4$ eV are not "real lines" but instead are degenerate having a zero imaginary part.) The "real lines" come in complex conjugate pairs and connect the bands; see Fig. 3. The way to loop through all the bands is simply to follow the labels presented here and in Fig. 3. Note that roots $r10$ and $r11$ lie outside the zone and are neglected in the calculations. All of the remaining roots are retained.

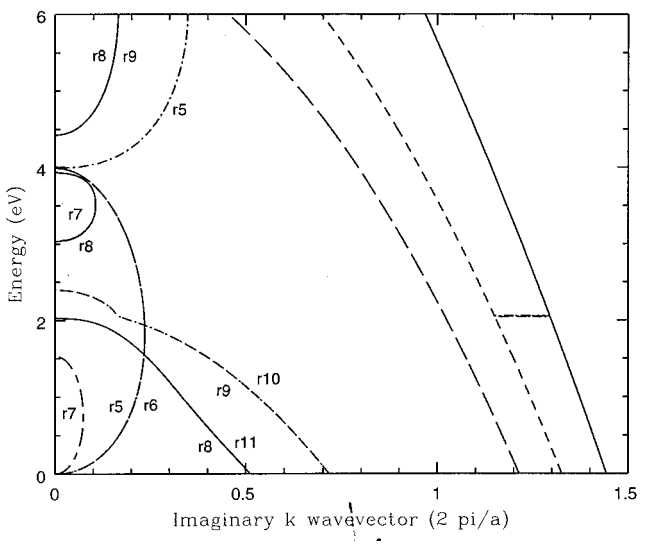

FIG. 3. Energy vs the imaginary part of k_z at $k_x=k_y=0$ for GaAs. See Fig. 2 for an explanation of the symbols. The curves at the extreme right of the figure are not included in the calculations, as they connect to bands that lie well above the highest energy considered. Note that only the positive imaginary bands are displayed except in the case of the "real lines" where both labels are shown to facilitate comparison with Fig. 2. The kink in roots $r9$ and 10, near 2 eV, is a result of imperfect band fitting.

duce the bands with the proper energies and slopes at the zone edge we are interested in, namely, the X point. These bands include not only the propagating (real) bands but also the evanescent (complex) bands, both of which have to be tracked carefully as the wave vector and energy vary.

We integrate our current densities over total energy E, and parallel wave vectors k_x and k_y. The reason for this will be apparent shortly. Hence, we need to determine the corresponding propagation wave vector along the growth axis k_z, as a function of k_x, k_y, and E. This is readily obtained from the $\vec{k}\cdot\vec{p}$ secular equation. Furthermore, we are interested in not only the real but also the complex k_z, i.e., the evanescent bands. This is because the imaginary parts of these complex k points are what connect the real bands together; the "real lines" as defined by Heine.[45] It is crucial to include them in the analysis, if a proper investigation of the electron propagation through the semiconductor is to be undertaken. For example, if the injected electron energy lies between the real bands, in the so-called forbidden zone, then the associated propagation wave vector k_z at that energy has a nonzero imaginary part.

We use a singular value decomposition[30] of the full-zone Hamiltonian matrix—one decomposition for each of the $n=1, 2, \ldots, 15$ roots $k_z^{(n)}$ of the secular equation—to obtain the set of full-zone, basis expansion coefficients.[44]

2. Construction of the semiconductor transfer matrices

We employ standard techniques to construct the transfer matrices.[25–27] The entire system (see Fig. 1) is partitioned into layers sufficiently thin so that in each layer the flat potential approximation is used to determine the wave propagation vectors and full-zone basis expansion coefficients. The wave functions (calculated in Secs. III C 1 and III C 3), taking into account the potential in each layer, are then matched at each of the two respective layer interfaces and the corresponding matching coefficients are factored out, yielding the transfer matrix for that layer. (For how these transfer matrices are used to obtain the transmission and reflection coefficients see Sec. II C 4.)

There are three items that determine the size (dimensions) of the transfer matrices. One is the number of basis state xy projections onto the layer interface planes. This number is readily obtained from examination of the 15 plane waves used to construct the symmetrized Γ-point basis wave functions.[38] Inspection of these waves reveals nine xy projections. Given in terms of the associated reciprocal lattice vector components they are [00], [11], $[1\bar{1}]$, $[\bar{1}1]$, $[\bar{1}\bar{1}]$, [20], [02], $[\bar{2}0]$, and $[0\bar{2}]$. The second item is the number of boundary conditions (BC's) used to match these projections across the interface. Here we use 2 BC's (see Sec. II A). Thus, for nine parallel momentum components we have a total of 18 BC's.

The remaining item is the number of accurate $k_z^{(n)}$ solutions (bands) that are available. To determine this, we examine our fitted complex band structure in Figs. 2 and 3. We observe that the number of bands depicted is less than the total 15 bands in our approximation. This discrepancy in the number of nonzero $k_z^{(n)}$ solutions and the total number of basis wave functions is to be expected, however, because many of the higher-energy bands do not have any direct con-

nection whatsoever to the lower-energy bands in the figures; the corresponding complex $k_z^{(n)}$ or ''real lines,''[45] which connect the real bands together, connect these higher-lying energy bands to others that are well in excess of the energies depicted.

Taking into account both the real and imaginary bands, these figures show that we have five accurate solutions of $k_z^{(n)}$ over the given E range (those bands labeled $r5$ through $r9$ in Figs. 2 and 3). The bands with the large imaginary wave vectors to the far right of those depicted in the respective imaginary band figures that are not labeled, however, are not considered. This is because these originate from bands well above the lowest Γ-X_3 conduction band that are not accurately fitted, and do not have the correct zero slope at the Brillouin zone boundary. Only the valence Γ-X_1, Γ-X_3, and Γ-X_5 band edges and the lowest conduction Γ-X_1 and Γ-X_3 band edges have been accurately fitted over the energy range depicted, as well as the corresponding slopes having been adjusted as near zero as is practicable.

Although we have nine wave functions, only the five associated with the fitted bands are reliable. This is consistent with having chosen only five plane waves and neglecting the [002] set. The larger plane-wave set is used to ensure the accuracy of the smaller basis set. Hence, we drop from further consideration the [002] set of plane waves, thereby achieving a consistent set of wave functions and wave matching coefficients, i.e., an equal number of each to carry out the boundary condition matching and subsequent construction of the transfer matrices.

3. Wave functions in the remaining materials

To facilitate boundary condition matching, the plane-wave states employed in the semiconductor are used to approximate the wave functions in the remaining BEEM components, i.e., in the STM tip, vacuum, oxide, metal overlayer, and collector electrode. (All metals are approximated by the free-electron model for Au and therefore we have not included the effects of the metal band structure.[46]) The corresponding bands in each of these components, with the exception of the vacuum, are all taken to be flat and not distorted by the applied bias (the oxide is assumed to be thin). There are no distortions because all the applied bias potential is dropped entirely across the STM vacuum by construction in BEEM.[1,2]

Scattering effects in the metal overlayer and oxide are incorporated into the model in the same manner as was done in the semiconductor. The metal overlayer, assumed to be Au, has a mean free path length of order 120 Å,[4] and typical thicknesses in the range from 50 to 100 Å. In the oxide case very limited data are available. No scattering length data are available so a range of ''reasonable'' values is considered. As for the oxide thickness, it depends critically on how clean the semiconductor surface is prior to metal deposition, and to some extent on how much interdiffusion occurs between the metal and the semiconductor. From Ref. 47 we find that a ''clean'' surface would be expected to have an oxide layer thickness of the order of 20 Å. We assume that the semiconductor surface can be taken to be ''clean'' and take the oxide layer to have a thickness of 20 Å.

The vacuum potential between the STM tip and the metal overlayer is modeled by the potential along the symmetry axis between a charged sphere and a ground plane.[48] This potential, by symmetry, depends only on the radius of the sphere and its distance from the plane. When the tip radius is comparable to or greater than the tip/metal-overlayer separation, the potential drop is nearly linear along the symmetric axis, analogous to the potential drop between parallel plates, as would be expected. On the other hand, when the tip radius becomes less than the tip/metal-overlayer separation, the potential drop is quite nonlinear.

This model should be an improvement over parallel plane models and should yield a better current dependence on tip distance, which is essential for the constant-current mode.

Finally, these wave functions are then used to construct the corresponding transfer matrices in each material exactly as in the semiconductor (see Sec. II C 2).

4. Derivation of the transmission and reflection coefficients

Rather than eliminating all the wave matching coefficients at each interface to obtain the composite transfer matrix coupling all the different materials together,[25–27] we instead use the regrouping technique of Schulman and Ting[49] to determine these coefficients. We do this so that we may increase the physical size of the semiconductor material we can consider before numerical instability creeps into the derivation of these matching coefficients. From these wave coefficients, we then determine the transmission and reflection coefficients in the standard manner[50]—averaging them over a unit cell to remove the remaining xy spatial dependency in these coefficients.

D. *L*-point transmission coefficient analysis

Analysis of the L-point transmission coefficient proceeds in essentially the same fashion as in the Γ- and longitudinal X-point cases with two exceptions. First, $\vec{k}$ changes direction to $G(111)/2$ requiring new $\vec{k}\cdot\vec{p}$ momentum matrix fitting elements along the Γ-L direction. And second, each injected electron must experience a significant scattering event(s), somewhere along its journey from the STM tip to the semiconductor, in order that the electron have the proper parallel (to the interface) momentum components required to access the semiconductor L point. This is because the STM tip injects all electrons essentially along the (001) growth axis direction due to the STM tip focusing.[1,2] The relative orientation of the L point to the growth axis (001) then requires a large change in k_x and k_y. (In contrast, the Γ and longitudinal X points both lie along the growth axis, and therefore such scattering events are not required.) The required scattering occurs either in the metal overlayer and/or at the metal-overlayer/semiconductor interface, and can be either elastic or inelastic. However, due to the typically thin metal overlayer (50–100 Å), it is expected that the majority of the scattering occurs at the metal-overlayer/semiconductor interface due to rough surface scattering.

We estimate an upper bound on the current due to scattering, by assuming that *all* the electrons have scattered into states with the proper parallel momentum components to ac-

cess the semiconductor L point through the interface. We have found that the resulting L-point collector-current estimate is negligible compared to the previously determined Γ- and longitudinal X-point collector currents.

Specifically, we assume that the k_x and k_y components of all the electrons are equal to $G(0.5, 0.5)$, the required L-point parallel momentum components, throughout all the BEEM structures. The k_z wave vector component is not restricted. The corresponding k_z's obtained with $k_x = k_y = 0.5G$, using the band fitting parameters obtained along the Γ-L direction, yielded four of five k_z's with large imaginary parts—three to four times the Γ-point k_z's. [We use five bands, k_z's, for the same reasons we did in the Γ- and longitudinal X-point cases (Sec. II C 2).]

The calculation yields a negligible L-point collector current in comparison to the Γ-point current—at least 10 orders of magnitude less. The dominant contributing factor is the relative size of the imaginary wave vector components, as compared to the Γ- and longitudinal X-point case. Thus, we neglect in our further consideration the contribution of the L-point current to the total BEEM collector current.

E. Transverse X-point transmission coefficient analysis

As in the L-point case, we anticipate that very little collector current will be contributed by these points. Similarly, we seek an upper bound estimate for the corresponding threshold behavior.

We use the symmetrized combination of plane waves that correspond to the X-point threshold bands of interest, namely, the conduction band (CB) edges X_1 and X_3, and the valence band (VB) edge X_5 at this point built from the set of four [011] plane waves (Ref. 38, Table VI).

We treat the two CB's, which lie approximately 0.4 eV apart at the X point in GaAs, as the current carrying bands, and the single degenerate VB, which lies nearly 5 eV below the X_1 band,[35] as a perturbation on these two CB's. We use nondegenerate $\vec{k}\cdot\vec{p}$ perturbation theory[44] to couple the X_1 and X_3 bands to the degenerate X_5 band in first order in the wave functions. The X_1 and X_3 bands are close enough in energy that the $\vec{k}\cdot\vec{p}$ perturbation approach yields reasonably small k_z values near threshold for both bands. On the other hand, the X_5 band is so far away in energy at the BEEM threshold at this point that the corresponding k_z estimated for this band will not be small, so a perturbation treatment of this VB is not valid.

The boundary conditions used here are a slight modification of the standard Ben Daniel–Duke BC's.[51] These standard BC's have been appropriately modified to include nonparabolic effective masses[52] in the semiconductor.

Scattering effects are overestimated again by assuming *all* electrons to have parallel momentum of $G(01)$ along the interfaces.

The calculation results in a transverse X-point collector current at threshold that is negligible in comparison to the Γ-point current. Specifically, the values obtained are more than ten times smaller than the typical noise detection threshold levels of 0.1 pA.[53] Thus, we neglect in our further consideration the contribution of the transverse X-point current to the total BEEM collector current.

F. Effective tip area

To estimate an effective tip area in our model to convert the calculated current densities to currents, we examined the potential distribution between the STM tip and the metal-overlayer plane to obtain an estimate of the breadth of the potential distribution. These calculations were carried out and yielded ambiguous results, i.e., there was no clear demarcation observed in the tip field lines where one could say that the tunnel current was confined. We shall simply assume that the effective tip area is given by πr_{tip}^2, where r_{tip} is the tip radius. This is at least correct in order of magnitude and has roughly the correct tip radius dependence. Unless otherwise specified, the tip radius is taken to be 20 Å—a typical value found in the literature.

It is worth noting that, in either the constant-height or constant-tunnel-current mode, not only does the effective tip area play the role of determining the current magnitude from the current densities [e.g., Eq. (1)], but also the corresponding effective tip radius determines the intensity of the electric fields between the tip and the metal-overlayer plane, and therefore the magnitude of the intervening vacuum potential (see Sec. II C 3). These two tip effects compete in the sense that decreasing the tip radius increases the tip field strength, thereby reducing the vacuum potential, but decreases the effective tip area, decreasing the injected current. At all but the highest bias levels, the tip area effects dominate over the tip electric field effects because the curvature induced in the vacuum potential, relative to a linear potential drop, does not become significant until the bias voltage approaches a substantial fraction of the vacuum barrier height (typically 2 V or more). When this occurs, the effective width of the barrier is greatly reduced, most notably in the mid-portion of the vacuum potential.

In the constant-height mode, this competing behavior is important in determining the magnitude of the collector-current. On the other hand, in the constant-tunnel-current mode, this behavior is not nearly as important because of the feedback built into this operating mode. This is because the vacuum width is adjusted accordingly until the preset tunnel current is obtained, irrespective of the effective tip area. For example, using the model in constant-tunnel-current mode and the effective tip area assumed above, it is observed that changing the tip radius from 10 to 100 Å increases the relative collector-current magnitudes by approximately 10% at the high end of the bias range—approximately 2 V. This is not a large change given the drastic change in the effective tip radius. What does change noticeably in the constant-tunnel-current mode in this case is the tip/plane separation. This width increases significantly when a larger tunnel tip radius is employed or decreases significantly when a smaller tunnel tip radius is employed. In this example, the corresponding vacuum width changes from roughly 5 to 7 Å, in good agreement with observation.[54,55]

III. MODEL RESULTS

The apparent threshold voltage (ATV), which will be referred to extensively in the following sections, is defined to be that voltage where the BEEM collector current I_c is just detected above the background noise level, exactly as it would be determined in an experiment. A typical BEEM current measuring noise limit lies in the range of 0.1 to 0.5 pA.[53] The lower limit of this range is used to determine the ATV.

A. Base-line data definition

The experimentally controllable BEEM parameters (doping, temperature, metal-overlayer thickness, etc.) take on a wide range of values in the literature. We chose values for the corresponding model input parameters that are frequently observed and used them to define a base-line *I*-*V* result. We then used this result to determine what effects varying these input parameters has on the calculated *I*-*V* curves. Our model base-line input parameters are presented in Table I. Note that the choices for the semiconductor cutoff and the scattering lengths were discussed in Sec. II B.

Additionally, the location of the metal-overlayer/semiconductor interface in relation to the leading semiconductor atomic plane within a unit cell needs to be specified. Since our basis set is finite, the calculated current results are dependent on the interface plane location for the wave-function matching. A similar dependency was found by Sham and Nakayama.[56] Using their results as a guide, we chose the relative distance between the nearest semiconductor crystal plane and the metal-overlayer/semiconductor interface to be halfway between the two GaAs sublattices. However, because our basis functions are expanded about the conventional origin[38] this choice shifts the interface location onto a lattice point.

To save space, the base-line BEEM collector current, tip separation, and base current spectra—using the input in Table I—are presented in Secs. III B 5, III B 4, and III B 6, respectively. [Note that neither the *L*-point nor the transverse *X*-point (100) data are included in these results since they are negligible.] The ATV is seen to be approximately 980 mV. Recall that the input value of the Schottky-barrier height is 900 mV. This apparently slightly higher threshold voltage is attributed primarily to the effects of the short scattering length, which reduces the collector current, yielding a higher ATV. For comparison, a longer scattering length of 250 Å yields an ATV approximately 60 mV below the input Schottky-barrier height due to the reduced scattering and the corresponding increase in the collector current. The longitudinal *X*-point (001) threshold occurs somewhere in the neighborhood of 1.4 to 1.45 V. (Higher voltage resolution is needed to pin down this threshold.) This range is consistent with what one would expect based upon the GaAs band structure.

B. BEEM model results

In each of the following data comparisons we change one parameter at a time in the base-line input data given in Table I. The salient results are discussed. All calculated or measured data points are simply connected by line segments for ease of viewing.

TABLE I. Base-line code input for Au/GaAs(001). With the exception of the semiconductor inelastic mean free path length, all the physical parameters listed having to do with the BEEM materials or equipment are fixed experimentally.

Temperature (K)	300.0
STM tip Fermi energy E_F (eV)	5.51
Fixed tunnel current (nA)	1.0
STM tip radius (Å)	20.0
Initial tip separation (Å)	4.7
Vacuum barrier height relative to E_F (eV)	4.3
Metal-overlayer thickness (Å)	70.0
Oxide layer contribution (1/0) ?	0
Semiconductor lattice constant (Å)	5.65
Number of vacuum transfer matrices	35
Minimum applied bias voltage (V)	0.7
Maximum applied bias voltage (V)	2.0
Number of voltage points	13
Semiconductor energy gap at zero temp (eV)	1.53
Semiconductor energy gap at input temp (eV)	1.43
Schottky-barrier height relative to E_F (eV)	0.9
Acceptor doping level ($/cm^3$)	1.0×10^{14}
Acceptor ionization energy (meV)	30.0
Donor doping level ($/cm^3$)	2.2×10^{17}
Donor ionization energy (meV)	5.0
L-band CB edge contribution (1/0) ?	0
Transverse *X*-band CB contribution (1/0) ?	0
Semiconductor dielectric constant	13.13
Natural Schottky-barrier width (Å)	757.5[a]
Barrier evaluated at every ? nd lattice point	2
Schottky-barrier-cutoff thickness (Å)	50.0[b]
Number of Schottky-barrier transfer matrices	4
Additional Schottky-barrier tail thickness (Å)	56.5[c]
Total Schottky-barrier thickness (Å)	101.7
Semiconductor inelastic mean free path (Å)	120.0
Metal elastic mean free path (Å)	120.0

[a]Width corresponds to z_b defined in Sec. II B.

[b]Rounded to the nearest multiple of the semiconductor lattice constant.

[c]Thickness is in multiples of the semiconductor lattice constant.

1. Doping

In Fig. 4 we present the BEEM spectra as a function of doping. (The low-voltage sampling resolution used here and elsewhere was needed to keep the length of a given code run down to a few days. Furthermore, the larger error bars at high voltages reflect the limited integration sample size; the integration region increases with voltage.) The doping dependence of the semiconductor scattering lengths l_f are determined from Eq. (8).

There are two competing effects present in the results. First, increasing the doping decreases the Schottky-barrier

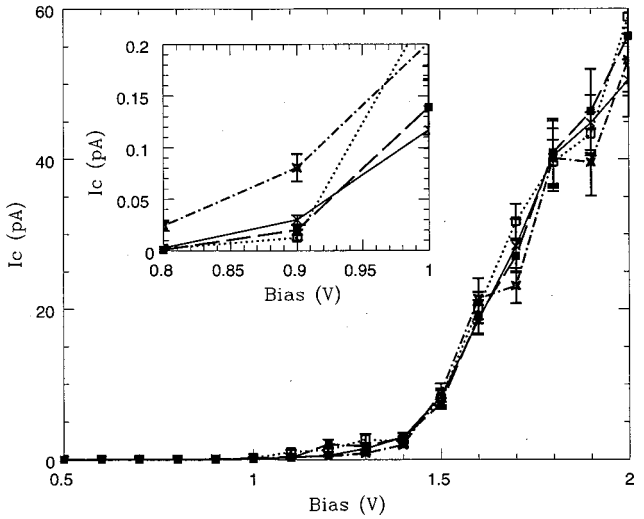

FIG. 4. BEEM collector-current spectrum as a function of the doping N_D. Collector current over a typical bias range and near threshold (inset). Dot-dash, $N_D=1.0\times10^{18}/\mathrm{cm}^3$, semiconductor scattering length $l_f=96$ Å; solid, $N_D=2.2\times10^{17}/\mathrm{cm}^3$, $l_f=120$ Å (base line); dash, $N_D=3\times10^{16}/\mathrm{cm}^3$, $l_f=161$ Å; dot, $N_D=3\times10^{15}/\mathrm{cm}^3$, $l_f=224$ Å.

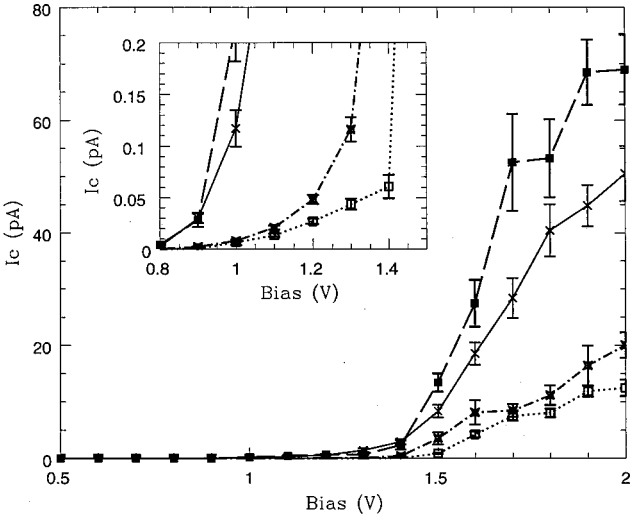

FIG. 5. BEEM collector-current spectrum as a function of the temperature T. Collector current over a typical bias range and near threshold (inset). Dot-dash, $T=500$ K, semiconductor scattering length $l_f=48$ Å; solid, $T=300$ K, $l_f=120$ Å (base line); dash, $T=77$ K, $l_f=1390$ Å; dot, $T=4.2$ K, $l_f=44$ Å.

width and increases the tunneling through the barrier decreasing the ATV. And, second, increasing the doping increases the impurity scattering in the semiconductor, increasing the ATV. The important point to note in the results is that the ATV is clearly a function of doping, even though the actual Schottky-barrier height used in the model is held fixed at 900 mV in all these cases. For comparison, when the scattering length is kept at the base-line value for all doping levels, the threshold voltage decreases monotonically with increasing doping. Beyond the threshold, the overall *I-V* curve does not depend sensitively on the doping variation. (The peak near 1.3 V at the lower doping levels is due to the longer semiconductor scattering length. With increased scattering length there are generally more peaks and valleys in the corresponding transmission coefficient, thereby increasing the chances of sample biasing in the integration.)

Contrast our results with the earlier BEEM model results (e.g., Ref. 2), where the effects of doping are not explicitly accounted for in any fashion, but rather only implicitly via fitting of the Schottky-barrier height and an overall scale factor. Scattering effects would also have to be accounted for by these fitting parameters. Since tunneling effects are completely ignored in these earlier models, these models would likely predict a lowering of V_b as the doping was increased.

2. Temperature

In Fig. 5 we present the BEEM spectra as a function of temperature. The semiconductor scattering lengths are determined from Eq. (8).

As in the doping case, there are two competing effects in the data. First, increasing the temperature from near absolute zero to room temperature and above decreases the Schottky-barrier width and increases its curvature. And, second, changing the temperature changes the mean free path length in the semiconductor. However, the temperature effect on the Schottky barrier is much less dramatic than the corresponding effect of changing the doping. On the other hand, the mean free path displays much more dramatic changes as regards temperature than as regards doping. This is readily observed in Fig. 5, in the increase in the ATV for both the very low- and very high-temperature cases, as compared to the $T=77$ K data.

Observe that the magnitude of the ATV change can be explained without recourse to a change in the Schottky-barrier height as a function of temperature, as is sometimes observed in the literature.[57] This is not to say that there is no Schottky-barrier height change due to temperature, but rather that its contribution, as suggested by our model results, is small. Indeed, the change in the measured threshold voltage given in the literature[57] at low temperature is significantly larger than can be explained by simply attributing this change solely to the Schottky-barrier height as determined from self-consistent barrier calculations. Our results suggest instead that the ATV change as a function of temperature can be primarily attributed to the large change in the mobility, or the corresponding change in the semiconductor scattering length.

We have not included the effects of temperature on the GaAs band structure, which may of course influence the above conclusions. Nor have we included the temperature effects on the metal-overlayer scattering length.

3. Metal-overlayer thickness

For the two smallest metal-overlayer thicknesses in Fig. 6 there is very little overall difference in the BEEM spectra, except near the threshold voltage. This is to be expected since both these thickness are significantly smaller than the Au metal-overlayer scattering length of 120 Å.[4] As the metal thickness approaches the metal-scattering length, as in the

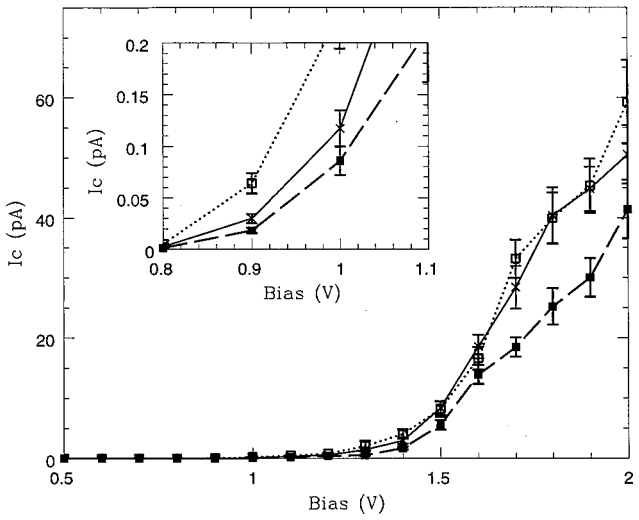

FIG. 6. BEEM collector-current spectrum as a function of the metal-overlayer thickness b. Collector current over a typical bias range and near threshold (inset). Dot, $b=50$ Å ; solid, $b=70$ Å (base line); dash, $b=100$ Å . The Au metal-overlayer scattering length $\lambda=120$ Å . (Ref. 4).

100 Å case, the collector current drops appreciably. This thickness dependency of the collector current is more apparent near the threshold voltage. Also observe that the metal scattering has affected the shape of each spectrum. This is in contrast to the simple scale change predicted by the earlier BEEM models.

In addition to the effects of scattering, another effect of changing the metal-overlayer thickness is that the resonances of the quasiwell formed between the STM vacuum and the metal/semiconductor interface change.[58] Recall that these structures are coupled in our model via application of boundary conditions. This may in part be responsible for the

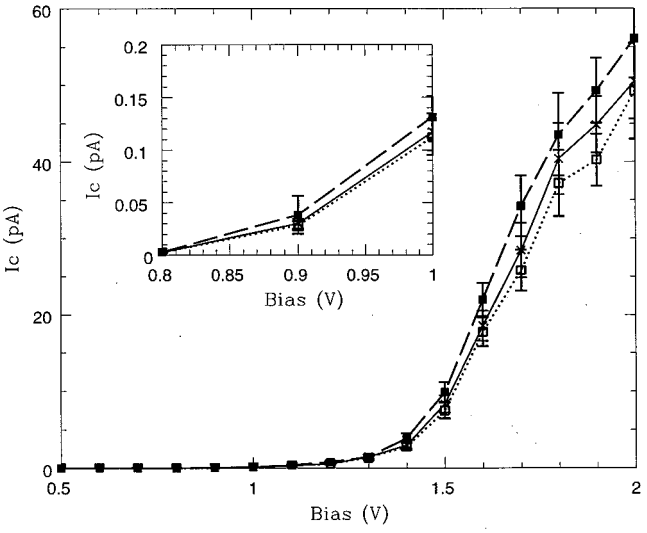

FIG. 7. BEEM collector-current spectrum as a function of the tip radius ρ. Collector current over a typical bias range and near threshold (inset). Dash, $\rho=100$ Å ; solid, $\rho=20$ Å (base line); dot, $\rho=10$ Å .

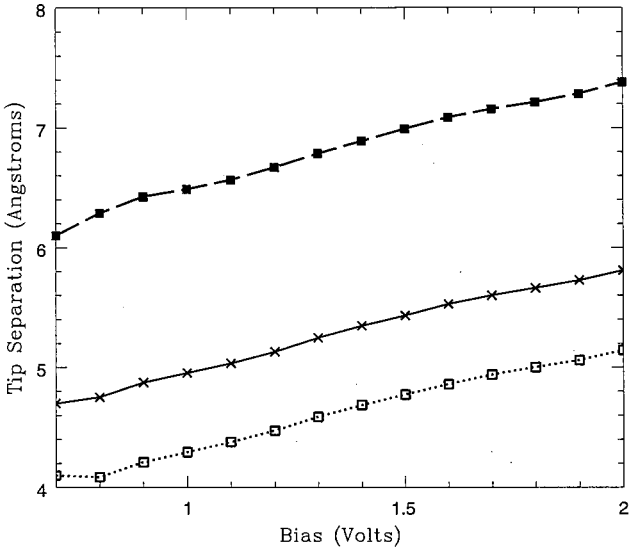

FIG. 8. Tip separation as a function of the tip radius ρ. Dash, $\rho=100$ Å ; solid, $\rho=20$ Å (base line); dot, $\rho=10$ Å .

change in shapes observed. Such an effect is entirely absent from all the previous BEEM models.

4. Tip radius

Figure 7 shows that there is little dependence of the constant-tunnel-current BEEM spectra on STM tip radius for voltages less than 1.5 V, and only a slightly larger variation of the order of 10% thereafter. In fact, all the remaining data lie within the error bars of the base-line data. What has changed markedly here, in contrast to all the previous results, is the STM tip separation exactly as indicated earlier in Sec. II F. The effective tip area was taken to be proportional to the square of the actual tip radius. Thus, in going from a 10 to a 100 Å tip radius, we expect an approximate 100-fold increase in the corresponding collector and tunnel currents. However, because of the constant-tunnel-current feedback in our model, the tip in this case has been moved 2 Å further away from the metal overlayer (Fig. 8) to compensate for this large current change. The magnitude of this tip shift is in good agreement with observation.[54,55]

On the other hand, for the constant-STM-tip-height BEEM mode, the ratios of the resulting calculated collector currents would be approximately proportional to the ratio of the squares of the tip radii. Clearly, in this mode there would be a substantial difference in the calculated BEEM currents as compared to the feedback mode results presented here (see Sec. III B 6).

5. Tunnel current

Figure 9 shows that the spectra scale nearly the same as the tunnel current as expected. Near threshold, it is clear that the ATV is again a function of the parameter under investigation, in this case the magnitude of the tunnel current, exactly as observed in the doping, temperature, and metal-overlayer thickness cases.

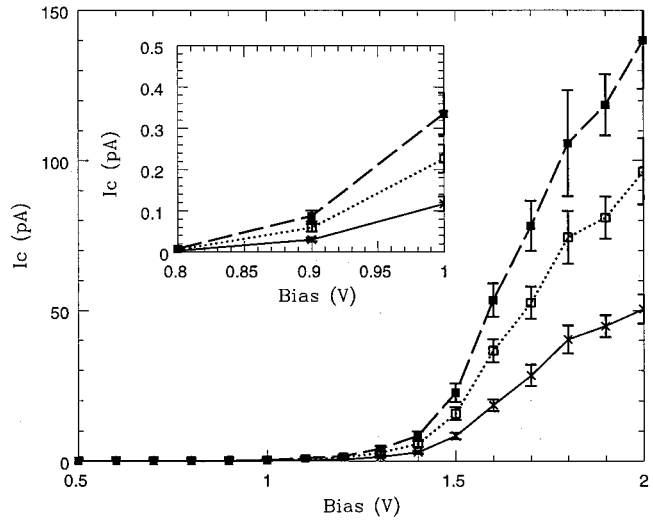

FIG. 9. BEEM collector-current spectrum as a function of the tunnel current magnitude I_t. Collector current over a typical bias range and near threshold (inset). Solid, $I_t=1.0$ nA (base line); dot, $I_t=2.0$ nA; dash, $I_t=3$ nA.

6. Constant-tip-height mode

In Fig. 10 we present the calculated collector and base currents as functions of bias voltage for both constant-tip-height and constant-tunnel-current modes.

In all but the threshold region, where the two modes were intentionally set up to be equal, it is clear that the addition of constant-tunnel-current feedback in the model has had a drastic effect on the corresponding collector and base currents. The large differences observed in these modes is a direct result of the tip separation changing a mere 1 Å over the voltage bias range depicted. Contrast our results with those of the Kaiser and Bell[2] model, which predicts very little sensitivity of the BEEM spectra to the tip separation in constant-tunnel-current mode.

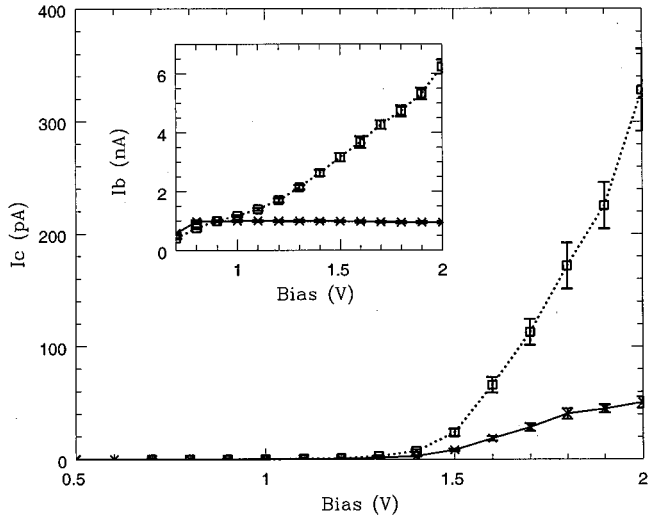

FIG. 10. Comparison of the BEEM collector and base currents in constant-tip-height and constant-tunnel-current modes. Collector and base (inset) current over a typical bias range. Dot, BEEM constant-tip-height mode; solid, BEEM constant-tunnel-current mode (base line).

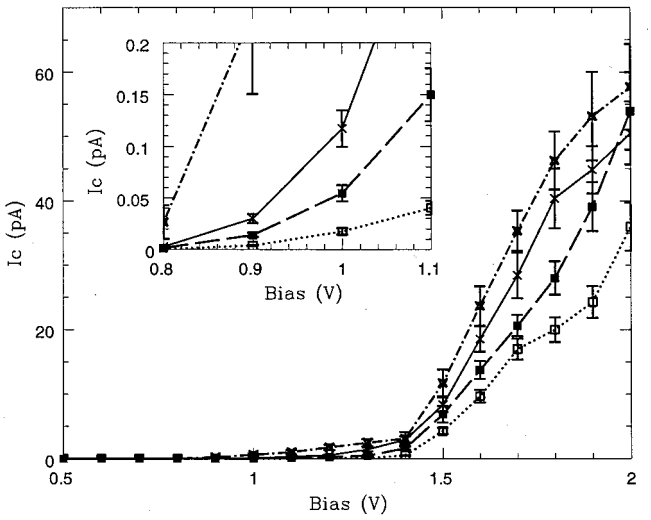

FIG. 11. BEEM collector-current spectrum as a function of the semiconductor scattering length l_f. Collector current over a typical bias range and near threshold (inset). Dot, $l_f=60.0$ Å; dash, $l_f=90.0$ Å; solid, $l_f=120$ Å (base line); dot-dash, $l_f=240$ Å.

Finally, observe that over the last 0.5 V of the bias range the feedback has completely changed the character of the respective collector currents, namely, that the feedback mode results suggest a leveling off, whereas the constant-tip-height mode results display no such analogous behavior. Indeed, the constant-tip-height mode data actually appear to be steepening near the end of this range.

7. Semiconductor scattering length

Figure 11 presents the BEEM spectra as a function of semiconductor scattering length. Clearly, the semiconductor scattering length has a profound effect on the overall collector-current spectra and is especially influential near threshold. Moreover, observe that the relative changes in the collector-current magnitude diminish with increasing scattering length in excess of the semiconductor cutoff length as expected (Sec. II B). Note that in most of the earlier models scattering is accounted for by an overall scale factor.[2] It is obvious that our approach to scattering has done more than simply scale the spectra.

It is sometimes claimed[59,60] that the variation of the apparent Schottky-barrier height V_b as a function of interface location x, i.e., $V_b(x)$, as deduced from the Kaiser and Bell based BEEM fitting models, is due to differences in the actual height of the barrier along the interface. In view, however, of the preceding results, it is also possible to interpret this observed functional dependency of $V_b(x)$ as a reflection of the level of scattering below the buried heterostructure interface and its effect on the *apparent* Schottky-barrier height, and not necessarily as an indicator of any variation of the *actual* Schottky-barrier height. A similar inference could also be drawn from the metal-overlayer scattering. If indeed $V_b(x)$ is due mainly to scattering rather than any actual

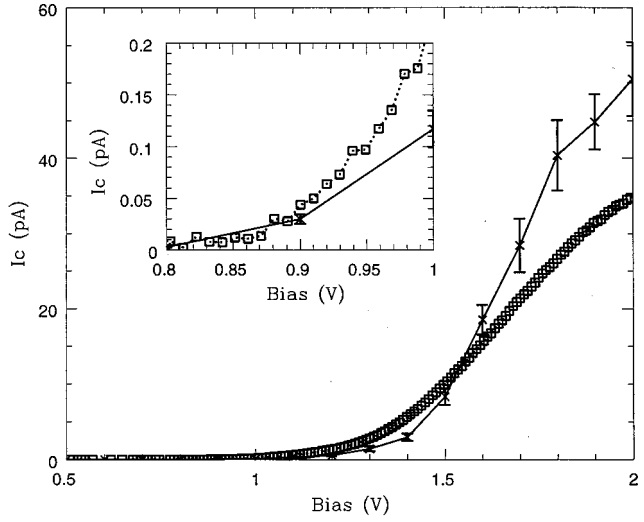

FIG. 12. Comparison of the measured and calculated BEEM Au/GaAs(001) collector-current spectra at $I_t = 1.0$ nA. Collector current over a typical bias range and near threshold (inset). Solid, calculated (baseline); dot, measured.

variation of the barrier height along the interface, then the resultant *I-V* curves at the various locations should have different shapes as indicated by our model.

C. Comparisons with experimental data

The measured data, provided courtesy of B. Morgan,[61] may be compared with the calculated tunnel spectra in Sec. III B 5 (Figs. 12–14). The general trend in each of these figures is that the theory underestimates the collector current below 1.5 V and overestimates it above 1.5 V. The rollover behavior in our results at the high end of the bias range is in general agreement with the measured data; in particular the

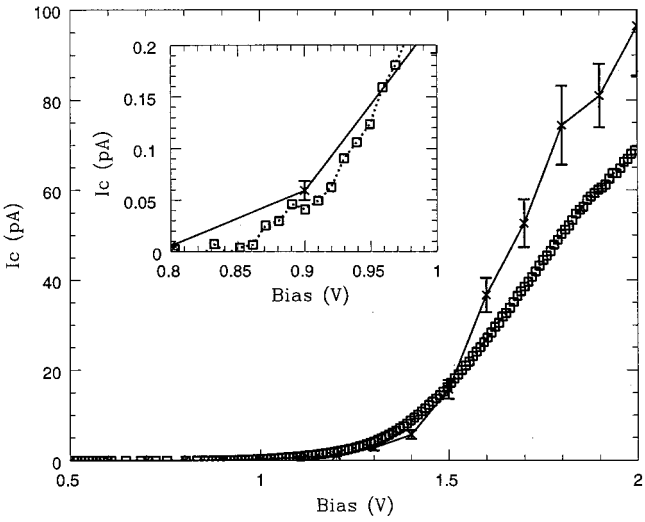

FIG. 13. Comparison of the measured and calculated BEEM Au/GaAs(001) collector-current spectra at $I_t = 2.0$ nA. Collector current over a typical bias range and near threshold (inset). Solid, calculated; dot, measured.

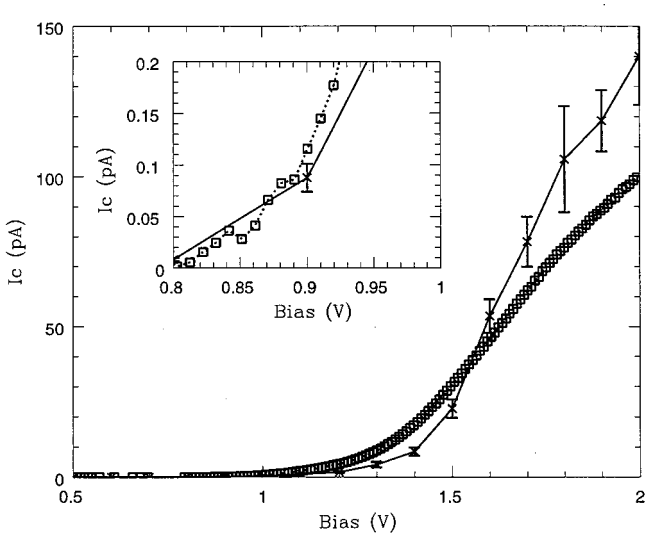

FIG. 14. Comparison of the measured and calculated BEEM Au/GaAs(001) collector-current spectra at $I_t = 3.0$ nA. Collector current over a typical bias range and near threshold (inset). Solid, calculated; dot, measured.

roll-off behavior becomes progressively weaker with increasing tunnel-current magnitude. Of the three data sets, the agreement between the collector currents with $I_t = 2.0$ nA appears to be the best. As for the apparent threshold voltage, it is seen that the difference between the calculated and measured values is approximately 30, 10, and 10 mV for Figs. 12–14, respectively. These differences are well within the neighborhood of the variations [$\leqslant \pm 50$ meV (Ref. 62)] typically observed from BEEM scan to scan on a given sample.

The corresponding dI_c/dV derivatives for these tunnel spectra—calculated using Savitzky-Golay smoothing filters[30]—are depicted in Fig. 15. (The voltage sampling had to be increased five-fold in the calculated data to obtain robust derivative results.) Overall, both sets of data display the same general behavior. In particular, both sets of data clearly display an inflection point in the 1.6–1.7 V range and subsequently display rollover behavior. These data are also in good agreement with the model of Kaiser and Bell.[2] Furthermore, both sets of data increase at approximately 0.9, 1.2, and 1.4 V; the last increase becomes more apparent on a larger plot scale. (The dI_c/dV model features are robust—in the sense that the overall features of the curve remain intact and in the same general position with regard to changes in the Savitzky-Golay smoothing sampling and the degree of the polynomial fitting[30] over a reasonable range of values.)

Kaiser and Bell[2] suggest that increases in dI_c/dV reflect BEEM voltage thresholds. If this is true, this suggests that our derivative data have picked up all three GaAs BEEM thresholds. Recall, however, that we found that the contribution of the *L* point to the total calculated collector current is negligible (Sec. II D).

To try to understand what is the source of the apparent *L*-point threshold in the model dI_c/dV results, we first examined what effect the feedback has on these results. We did this by turning off the feedback and switching over to

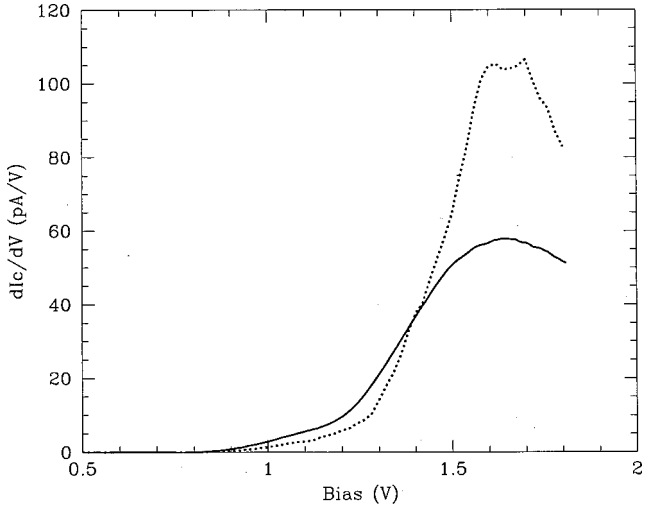

FIG. 15. Comparison of the measured and calculated dI_c/dV spectra at $I_t=1.0$ nA. Dot, model data; solid, measured data. The model dI_c/dV spectrum used $n_r=25$, $n_l=10$, and $m=4$ (fitting polynomial order) to carry out the Savitzky-Golay filtering (Ref. 30). The calculated curves terminate at 1.8 V due to an insufficient number of data points for proper smoothing beyond this bias range.

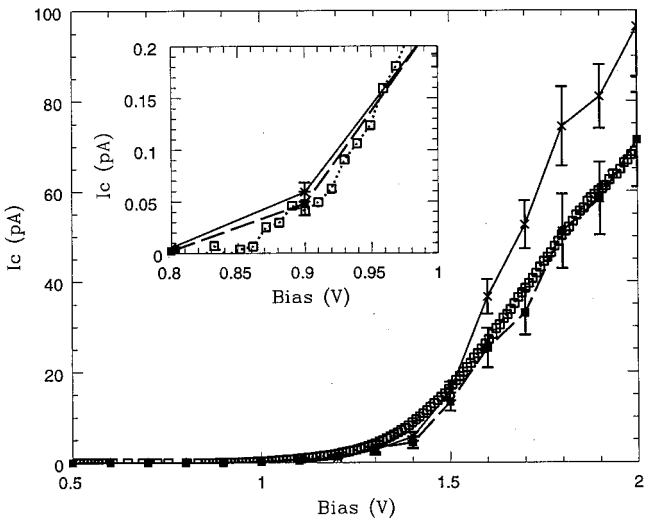

FIG. 16. Comparison of the base-line, adjusted base-line, and the measured BEEM collector-current spectra at $I_t=2.0$ nA. Collector current over a typical bias range and near threshold (inset). Solid, base line; dash, adjusted base line; dot, measured data.

constant-tip-height mode. Using the same model input parameters as before revealed that the feedback was not the source for the apparent L-point threshold, as the constant-tip height dI_c/dV results clearly displayed an increase near 1.2 V. (This result was also found to be robust in the same sense as discussed above.) Next we examined the I-V curves with the parameter changes that were undertaken previously and again found this same general behavior; although it must be pointed out that this examination was carried out with the lower-voltage sampling used in the base line, so some biasing of these results is possible.

Hence, by the process of elimination, we conclude that the source of the apparent L-point threshold is due not to an actual threshold, but rather to other band-structure effects and that the ATV at this point is simply a coincidence. Thus, the dI_c/dV data are not necessarily a good indicator of the Au/GaAs(001) L-point threshold.

Finally, to further improve the agreement between the calculated and measured data we took the liberty of adjusting various model parameters. Of all the model parameters that could be legitimately adjusted—that is, were not intrinsically fixed—changing the choice of the relative position of the metal-overlayer/semiconductor interface and the leading semiconductor atomic plane within a unit cell (see the discussion in Sec. III A) resulted in by far the best improvement in the overall agreement of the two data sets. The value was changed from the original $z=a/8$ to $z=a/10$, where a is the GaAs lattice constant. The results of this change, the adjusted base line, as well as the original base line and measured data for the 2 nA tunnel-current case are given in Fig. 16. The measured data lie within the calculated error bars over the majority of the bias range. In the other two tunnel-current data sets (1 nA and 3 nA), the agreement was significantly improved but not quite as much as in Fig. 16. Physical justification for such a change in the relative position of the metal-overlayer/semiconductor interface and the leading semiconductor atomic plane can be made by appealing to the oxide layer that lies in general between the metal and semiconductor.

IV. SUMMARY AND CONCLUSIONS

In summary, our model (Sec. II) includes both constant-tunnel-current feedback and calculation of the transmission coefficient beyond the EMA—including detailed symmetry treatments of the primary k-space points. Our results (Sec. III) indicate that virtually all the experimentally accessible model input parameters (doping, temperature, STM tip radius, tunnel-current magnitude, and metal-overlayer thickness), as well as the experimentally inaccessible model input parameters (scattering lengths and the semiconductor cutoff length) affect to some extent—in some cases significantly—the overall BEEM spectra characteristics, and in particular the threshold characteristics. It follows that a precise determination of the actual Schottky-barrier height from BEEM data must be inferred within the context of a model that includes realistic approximations of all these parameter effects. None of the earlier models, which all fitted the Schottky-barrier height, includes all the parameter effects described.

We also compared our results (Sec. III C) with a limited set of experimental data and found reasonably good agreement. In addition, we compared the corresponding dI_c/dV data and found that our data showed all the same qualitative behavior (inflection point and increases) very near the same voltages as in the measured data. What was surprising was that our model dI_c/dV data also clearly displayed an apparent L-point threshold near 1.2 V as did the measured data. However, we found the L-point contribution to the collector

current was negligible. By the process of elimination we were able to rule out feedback and the other model parameters as the source of the apparent L-point threshold, leaving only the band-structure effects. Hence, the apparent threshold at the L point is a coincidence. Consequently, we conclude that the dI_c/dV data are not a good indicator of where the band thresholds occur in the case of valleys with finite in-plane wave vectors.

ACKNOWLEDGMENTS

One of us (D.A.P.) wishes to thank Dr. J. Boisvert for many useful and stimulating discussions, and for the use of his code GAASFERM and Dr. Brent Morgan for graciously providing Au/GaAs BEEM data. Financial support was provided by NSF Grants No. DMR 97-21444 and No. DMR 94-21966.

[1] W. J. Kaiser and L. D. Bell, Phys. Rev. Lett. **60**, 1406 (1988).
[2] W. J. Kaiser and L. D. Bell, Phys. Rev. Lett. **61**, 2368 (1988).
[3] M. H. Hecht, L. D. Bell, W. J. Kaiser, and F. J. Grunthaner, Appl. Phys. Lett. **55**, 780 (1989).
[4] A. M. Milliken, S. J. Manion, W. J. Kaiser, L. D. Bell, and M. H. Hecht, Phys. Rev. B **46**, 12 826 (1992).
[5] L. D. Bell, M. H. Hecht, and W. J. Kaiser, Phys. Rev. Lett. **64**, 2679 (1990).
[6] M. D. Stiles and D. R. Hamann, Mater. Sci. Eng., B **14**, 291 (1992).
[7] M. D. Stiles and D. R. Hamann, Phys. Rev. B **38**, 2021 (1988).
[8] M. Prietsch and R. Ludeke, Phys. Rev. Lett. **66**, 2511 (1991).
[9] R. Ludeke and M. Prietsch, J. Vac. Sci. Technol. A **9**, 885 (1991).
[10] A. E. Fowell, R. H. Williams, B. E. Richardson, A. A. Cafolla, D. I. Westwood, and D. A. Woolf, J. Vac. Sci. Technol. B **9**, 581 (1991).
[11] T. Hasegawa, K. Takata, S. Hosaka, and S. Hosoki, J. Vac. Sci. Technol. B **9**, 758 (1991).
[12] P. Niedermann, L. Quattropani, K. Solt, A. D. Kent, and O. Fischer, J. Vac. Sci. Technol. B **10**, 580 (1992).
[13] A. A. Talin, D. A. A. Ohlberg, R. S. Williams, P. Sullivan, I. Koutselas, B. Williams, and K. L. Kavanagh, Appl. Phys. Lett. **62**, 2965 (1993).
[14] E. Y. Lee and L. J. Schowalter, J. Appl. Phys. **70**, 2156 (1991).
[15] L. J. Schowalter and E. Y. Lee, Phys. Rev. B **43**, 9308 (1991).
[16] E. Y. Lee and L. J. Schowalter, Phys. Rev. B **45**, 6325 (1992).
[17] H. D. Hallen, A. Fernandez, T. Huang, J. Silcox, and R. A. Buhrman, Phys. Rev. B **46**, 7256 (1992).
[18] W. J. Kaiser, M. H. Hecht, L. D. Bell, F. J. Grunthaner, J. K. Liu, and L. C. Davis, Phys. Rev. B **48**, 18 324 (1993).
[19] L. D. Bell, S. J. Manion, M. H. Hecht, W. J. Kaiser, R. W. Fathauer, and A. M. Milliken, Phys. Rev. B **48**, 5712 (1993).
[20] A. Bauer, M. T. Cuberes, M. Prietsch, and G. Kaindl, Phys. Rev. Lett. **71**, 149 (1993).
[21] L. Quattropani, K. Solt, P. Niedermann, I. Maggio-Aprile, O. Fischer, and T. Pavelka, Appl. Surf. Sci. **70**, 391 (1993).
[22] A. Bauer, M. T. Cuberes, M. Prietsch, and G. Kaindl, J. Vac. Sci. Technol. B **11**, 1584 (1993).
[23] J. G. Simmons, J. Appl. Phys. **34**, 1793 (1963).
[24] R. Ludeke, Phys. Rev. Lett. **70**, 214 (1993).
[25] A. Harwit, J. S. Harris, Jr., and A. Kapitulnik, J. Appl. Phys. **60**, 321 (1986).
[26] D. C. Hutchings, Appl. Phys. Lett. **55**, 1082 (1989).
[27] K. F. Brennan and C. J. Summers, J. Appl. Phys. **61**, 614 (1987).
[28] D. A. Pearson and L. J. Sham, Appl. Phys. Lett. **76**, 3989 (2000).
[29] For more details, see D. A. Pearson, Ph.D. thesis, University of California, San Diego, 1999.
[30] W. H. Press, S. A. Teukolsky, W. T. Vetterling, and B. P. Flannery, *Numerical Recipes in FORTRAN: The Art of Scientific Computing*, 2nd ed. (Cambridge University Press, Cambridge, 1992).
[31] R. P. Brent, *Algorithms for Minimization without Derivatives* (Prentice Hall, Englewood Cliffs, NJ, 1973).
[32] H. K. Henisch, *Semiconductor Contacts: An Approach to Ideas and Models*, Vol. 70 of *International Series of Monographs on Physics* (Oxford Science Publications, Oxford, 1984).
[33] S. M. Sze, *Physics of Semiconductor Devices*, 2nd ed. (Wiley-Interscience, New York, 1981).
[34] C. D. Thurmond, J. Electrochem. Soc. **122**, 1133 (1975).
[35] Numerical Data and Functional Relationships in Science and Technology, edited by O. Madelung, Landolt-Börnstein, New Series, Group III, Vol. 22, Pt. a (Springer, Berlin, 1987).
[36] D. L. Rode and S. Knight, Phys. Rev. B **3**, 2534 (1971).
[37] R. L. Petritz and W. W. Scanlon, Phys. Rev. **97**, 1620 (1955).
[38] F. Bassani, in *Semiconductors and Semimetals*, edited by R. K. Willardson and A. C. Beer (Academic Press, New York, 1966), Vol. 1, p. 21.
[39] M. Cardona and F. H. Pollak, Phys. Rev. **142**, 530 (1966).
[40] C. Kittel, *Introduction to Solid State Physics*, 5th ed. (Wiley & Sons, New York, 1953).
[41] J. R. Chelikowsky and M. L. Cohen, in *Basic Properties of Semiconductors*, edited by P. T. Landsberg (North-Holland, Amsterdam, 1992), Vol. 1.
[42] J. R. Chelikowsky, in *Quantum Theory of Real Metals*, edited by J. R. Chelikowsky, and S. G. Louie (Kluwer Academic Publishers, Dordrecht, 1996).
[43] J. R. Chelikowsky, T. J. Wagener, J. H. Weaver, and A. Jin, Phys. Rev. B **40**, 9644 (1989).
[44] E. O. Kane, in *Semiconductors and Semimetals* (Ref. 38), p. 75.
[45] V. Heine, Proc. Phys. Soc. London **81**, 300 (1963).
[46] F. J. Garcia-Vidal, P. L. de Andres, and F. Flores, Phys. Rev. Lett. **76**, 807 (1996).
[47] G. P. Schwartz, Thin Solid Films **103**, 3 (1983).
[48] P. Morse and H. Feshbach, *Methods of Theoretical Physics* (McGraw-Hill, New York, 1953), Part II, p. 1299.
[49] J. N. Schulman and D. Z. Y. Ting, Phys. Rev. B **45**, 6282 (1992).
[50] L. I. Schiff, *Quantum Mechanics*, 3rd ed. (McGraw-Hill, New York, 1955).
[51] D. J. Ben Daniel and C. B. Duke, Phys. Rev. **152**, 683 (1966).
[52] G. Brozak, E. A. de Andrada e Silva, L. J. Sham, F. DeRosa, P. Miceli, S. A. Schwarz, J. P. Harbison, L. T. Florez, and S. J. Allen, Jr., Phys. Rev. Lett. **64**, 471 (1990).
[53] Dr. Brent Morgan (private communication).
[54] G. Binnig and H. Rohrer, in *Scanning Electron Microscopy/1983/*

III, edited by G. M. Roomans (Scanning Electron Microscopy, Inc., Chicago, 1983), Part 3, p. 1079.
[55] Dr. Ed Yu (private communication).
[56] L. J. Sham and M. Nakayama, Phys. Rev. B **20**, 734 (1979).
[57] C. Eder, A. J. Smoliner, G. Strasser, and E. Gornik, Appl. Phys. Lett. **69**, 1725 (1996).
[58] H. Sirringhaus, E. Y. Lee, and H. von Kanel, Phys. Rev. Lett. **73**, 577 (1994).
[59] A. A. Talin, R. S. Williams, B. A. Morgan, K. M. Ring, and K. L. Kavanagh, Phys. Rev. B **49**, 16 474 (1994).
[60] A. A. Talin, R. S. Williams, B. A. Morgan, K. M. Ring, and K. L. Kavanagh, J. Vac. Sci. Technol. B **12**, 2634 (1994).
[61] Data provided courtesy of Dr. Brent Morgan of the University of California, San Diego, Electrical and Computer Engineering Department.
[62] M.-L. Ke, D. I. Westwood, C. C. Matthai, B. E. Richardson, and R. H. Williams, Phys. Rev. B **53**, 4845 (1996).